arXiv:2307.07887v1 [cs.CV] 15 Jul 2023

Handwritten and Printed Text Segmentation: A Signature Case Study

Sina Gholamian
Thomson Reuters AI Labs
Toronto, Canada
sina.gholamian@thomsonreuters.com

Ali Vahdat
Thomson Reuters AI Labs
Toronto, Canada
ali.vahdat@thomsonreuters.com

Abstract

While analyzing scanned documents, handwritten text can overlay printed text. This causes difficulties during the optical character recognition (OCR) and digitization process of documents, and subsequently, hurts downstream NLP tasks. Prior research either focuses only on the binary classification of handwritten text, or performs a three-class segmentation of the document, i.e., recognition of handwritten, printed, and background pixels. This results in the assignment of the handwritten and printed overlapping pixels to only one of the classes, and thus, they are not accounted for in the other class. Thus, in this research, we develop novel approaches for addressing the challenges of handwritten and printed text segmentation with the goal of recovering text in different classes in whole, especially improving the segmentation performance on the overlapping parts. As such, to facilitate with this task, we introduce a new dataset, SignaTR6K, collected from real legal documents, as well as a new model architecture for handwritten and printed text segmentation task. Our best configuration outperforms the prior work on two different datasets by 17.9% and 7.3% on IoU scores.

1. Introduction

For a variety of purposes, digitization of hard-copy documents and surrounding challenges are an active area of research both in academia [33, 19, 35, 18, 11, 28] and industry [26]. This digital transformation involves the scanning of paper documents through an OCR process that makes their text accessible for downstream natural language processing (NLP) tasks, such as named entity recognition (NER). The documents of interest may come from a variety of domains such as historical documents [35], legal and court-issued documents [26], business contracts [33], and medical records and prescriptions [10]. Although various studies have been conducted as listed above, there is yet a considerable gap between current approaches and human-level performance in mix-text scenarios (i.e., when handwritten and printed text overlap). For example, it happens often that attorneys sign legal documents, which causes their signatures to overlap with their information. This fact diminishes the performance of character recognition for OCR tools, and thus, causes difficulty for downstream tasks to correctly detect information associated with the attorneys and their law firms. Figure 1 shows an example of handwritten text (HT) and printed text (PT) overlapping for court documents. Extracting parties names is an important step in the named-entity recognition (NER) task in legal and court documents [32]. While attorneys and different parties sign the court documents and then they are scanned with OCR tools, the signatures often overlay and mask the names and law firms information. Because of this issue, semantic segmentation of handwritten (e.g., lawyers' signatures and accompanying handwritten text), and printed text, i.e., the lawyer and the law firm information, becomes important.

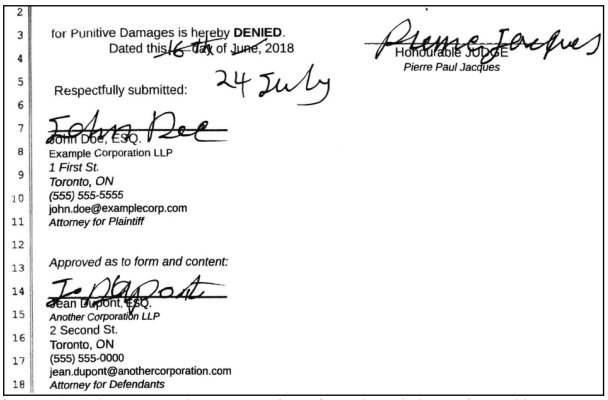

Figure 1: The court document is printed and then signed/annotated by different parties. This causes the handwritten text to overlay underlying printed information, and thus causes performance degradation on downstream tasks, e.g., named entity recognition (NER). This is a fabricated example, however very similar to the original documents, to protect personally identifiable information (PIIs).

In this research, we aim to tackle the challenges of HT and PT segmentation, as there is still a large gap between human-level performance and existing approaches for this task. Our focus in this effort is on improving the segmentation performance on overlapping regions for scanned legal documents, and for this purpose, we also

release a new dataset. In summary, our research makes the following contributions:

- We release a new dataset, SignaTR6K (pronounce as Signature 6K)[1] generated from 200 pixel-level manually annotated crops of images from original legal documents. The dataset contains signatures, handwritten text, and printed text that often overlap with each other. Using data augmentation, we create a dataset of sizes 5169, 530, 558, for train, validation, and test, respectively, that we release to public under a research-use licence, to facilitate dataset availability for further research and deep-learning segmentation models training and evaluation.
- We provide a novel architecture that combines both *semantic segmentation features* and *fine features* to improve the performance of text segmentation compared to the prior work. Additionally, we introduce a new loss function, *Fusion loss*, that, comparatively, is stable and convergences to the optimal loss values and Intersection over Union (IoU) scores [2].
- Lastly, we perform a comprehensive quantitative and visual evaluation of different variations of our approach against prior work on two different datasets, and illustrate our approach's superior performance in text segmentation task, especially on more difficult segmentation scenarios that printed and handwritten text overlap.

2. Background and Literature Review

Text segmentation problem is defined as: given a scanned document possibly containing handwritten, printed, and background (i.e., blank) pixels, assign each pixel to its corresponding class. Scanned documents can come from different sources such as hard-copy paper documents or microfilms [28, 35]. Formally speaking, for a given document D, assuming there exist three classes as handwritten text HT, printed text PT, and background BG, and pixel p_i: $\forall p_i \in D : p_i(c) == True\ if\ p_i \in c\ \&\&\ c \in \{HT, PT, BG\}$ (1). It can happen that a pixel belongs to two classes, i.e., both HT and PT classes when handwritten text overlays printed text, which single-label three-class formulation cannot handle this case.

Several prior research have aimed at tackling handwritten and printed text separation [11, 18, 28, 35], but they suffer from limitations. They either focuses on binary classification, i.e., whether a pixel is handwritten or not [18], or 3-class formulation of the problem, i.e., classifying each pixel as either handwritten, printed, or background [11, 28, 35]. This exclusive assignment of pixels to three different classes paralyzes any machine learning segmentation model to properly detect pixels in the overlapping areas to belong to both handwritten and printed classes. In our usecase scenario in Figure 1, the OCR process achieves insufficient performance due to overlapping of handwritten text and signatures that overlay the printed text. As such, to improve the documents digitization quality, and subsequently a wide range of downstream document understanding and natural language processing (NLP) tasks, it is vital to develop image processing approaches that can understand and properly segment different layers of text, i.e., printed and handwritten text.

Models. Prior literature have applied various approaches for handwritten and printed text identification and separation. Early approaches [12, 20] formulated the problem as a binary classification task, with KNN and SVM, and used connected component (CC) (i.e., group of pixels). More recently, Li et al. [22] applied conditional random fields (CRFs), with formulating both unary and pair-wise potentials for adjacent connected components by leveraging convolutional neural networks (CNNs) architecture for the separation of CCs. The problem with CC-based approaches is that it makes the class membership for the entire component (i.e., not pixel level). As such, pixel-level segmentation methods were proposed that leverage Markov random fields (MRFs) and MLPs [27, 30] for pixel-level classification of PT and HT segmentation. Upon the success of encoder-decoder architectures in object segmentation [29], more recent works [18, 11, 28, 35] have generally adopted a U-Net based architecture [29], that encompasses an encoder-decoder network, for HT and PT segmentation.

Besides our contribution in releasing a manually annotated dataset of legal documents containing overlapping text, SignaTR6K, our methodology is also different from prior works in multiple major aspects. First, we perform a four-class formulation of the segmentation problem, that allows the overlapping pixels to be assigned to a new class (OV) which means that both HT and PT layers are present, which improves the segmentation performance. Secondly, we propose a new architecture, a Mixed Feature Model (MFM), that combines a fine feature path (FFP) with a semantic segmentation path (SSP) and improves the performance by bringing in both high-level and low-level features. Prior work in U-Net style architecture [18, 11, 28, 35] only leverages the SSP path. We also introduce a new loss function, Fusion Loss, that convergences faster and is more stable compared to prior losses for HT and PT segmentation task. Moreover, we introduce a post-processing heuristic based on conditional random fields (CRFH) to perform relabling and further improve the text segmentation performance. Additional information on the related works and background is available in the appendices.

[1] Available at `https://forms.office.com/r/2a5RDg7cAY`

[2] A provisional patent has been filed for the systems and methods discussed in this paper and the proprietary nature of the implementation refrains us from releasing the code.

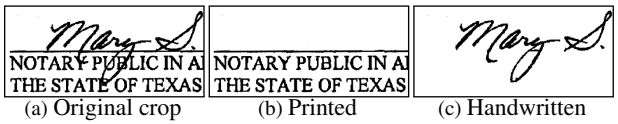

(a) Original crop (b) Printed (c) Handwritten

Figure 2: This figure shows a real crop from a legal document. (a) The original image containing printed text and overlaying handwritten signature; (b) Printed layer pixels annotated only; (c) Handwritten layer pixels annotated only. All pixels that are not present in printed or handwritten pixels are marked as background.

3. SignaTR6K Dataset

Successful training of a segmentation model requires the availability of high-quality datasets of labelled documents for training and testing. Due to the limited availability of public data that contains both handwritten and printed text, prior research has aimed to synthetically generate data by combining available datasets that contain only printed or handwritten text, such as IAM [25], RIMES [3], PRImA [9], CVL [21], Scanned Questionnaire [4], and WGM-SYN [35] datasets. The scanned documents may come from different domains with different fonts, characters and quality. Whether the original documents having poor quality in the case of archival documents [35], or the scanning process resulted in lower resolution or loss of contrast, these factors also add to the difficulty of the text segmentation task. In addition, in some cases errors are introduced in the automated labeling process [28]. As such, the lack of precisely and manually annotated and verified dataset from real sources that contains various patterns of overlapping printed and handwritten text makes the application of a supervised machine learning (ML) process even more difficult. As such, we introduce a new dataset, **SignaTR6K** (pronounced as Signature 6K), that is originated from 200 original legal documents from Thomson Reuters Legal Content Services [6], with overlapping printed and handwritten text, and hand-drawn signatures, e.g., Figure 1. The documents are manually labeled and verified.

Figure 2 shows an original crop from SignaTR6K, which includes a signature and the information of the signing party. Due to the presence of personally identifiable information (PIIs), we performed the crops to avoid any visible PIIs. Figure 2a shows the original image containing printed text and overlaying handwritten signature. Figure 2b shows printed layer pixels only, and Figure 2c contains handwritten layer pixels only that are manually annotated. All pixels that are not present in printed or handwritten channels are marked as background pixels. It is also clear that in overlapping scenarios, some pixels belong to both handwritten and printed layers.

Dataset Generation. As hand-annotating a large set of real documents is time-consuming and costly, in order to expand on the size of the dataset and make it sufficient for deep learning model training, we leverage data synthesis and augmentation approaches [18]. The synthetic approaches include general augmentation of crops, shifting, magnifying, and rotating. We also overlay handwritten and printed pixels from different crops to generate new real-like examples of overlapping text. For this purpose, out of the 200 distinct original document samples, in order to have mutually exclusive samples in the test set, we set aside 16 crops to be augmented only for the test set. We create training and validation sets from the remaining 184 samples. With this approach and after excluding generated samples with visible PIIs, we have curated a dataset for training, validation, and testing sets of sizes 5169, 530, and 558 samples, respectively. Each sample is a pair of gray-scale crop and its ground truth, which comes from manual annotations. Each image has a pixel sizes of 256 by 256 and in three channels (RGB) and typically contains several HT and PT overlaps. Four examples from SignaTR6K dataset are presented in Figure 3, with their gray-scale crops and their corresponding ground truth (GT) labels. HT is marked by green, PT by red, and BG by blue. The HT and PT overlapping pixels have both green and red channel values and, thus, are turned on as yellow. We envision that this dataset can be used for model training from scratch or further fine-tuning of a pre-trained classification or segmentation model for a specific task. The SignaTR6K will be made freely available to the public under a research-use-only license.

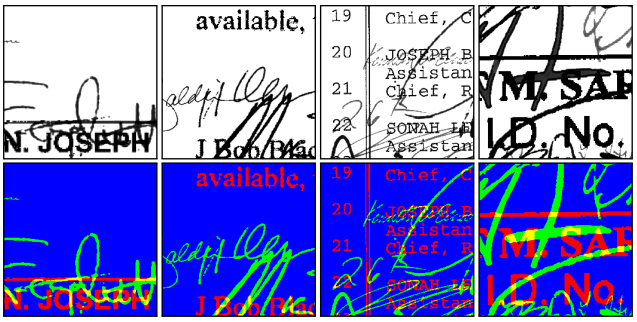

Figure 3: Examples from SignaTR6K dataset, with top row showing the crops and bottom row their ground truth annotations. Red: class PT, printed, Green: class HT, handwritten, and Blue: class BG, background.

4. Approach and Methodology

In this section, we explain our approach, reasons behind the architecture used, Semantic Segmentation Path (SSP) and Fine Feature Path (FFP), different loss functions used, and our introduced *Fusion* loss.

4.1. Model Architecture

The general architecture for object segmentation applies a U-Net architecture [29, 24]. This architecture leverages a fully convolutional network (FCN), that is without fully connected layers that are present at the end of convolutional neural networks (CNNs). The U-Net architecture consists of two main parts, an encoder and a decoder. In the

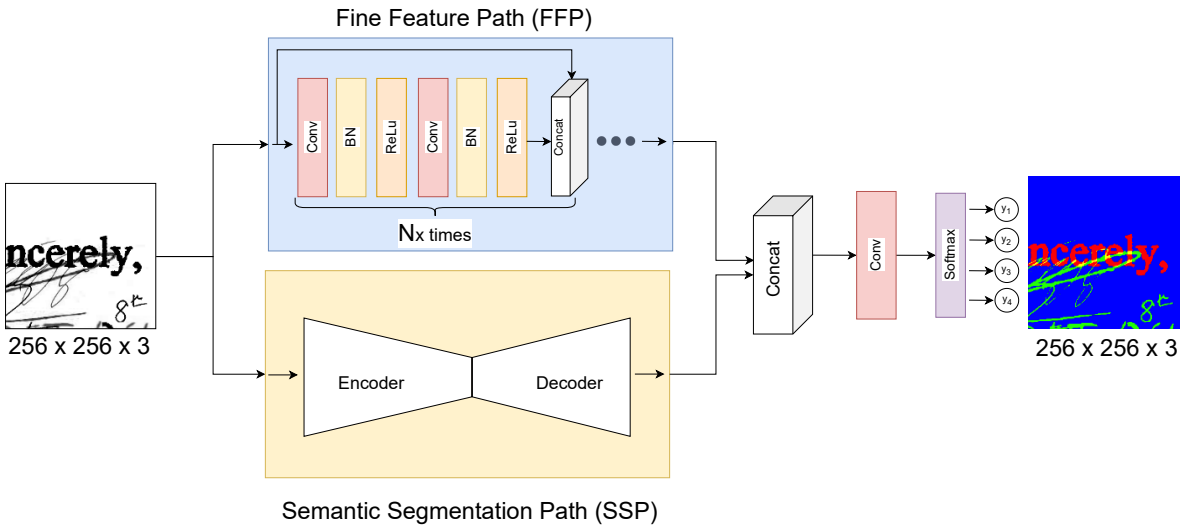

Figure 4: Our architecture proposal showing FFP and SSP model paths. The output of FFP and SSP are concatenated before the final round of convolutions and a Softmax activation is selecting on of the four classes for each pixel. The final output of the model is pixel-level annotations of the input image. BN: BatchNorm.

encoder part, the original image, in our case a document crop, is inputted to the model and goes through a set of convolutions and max-pooling layers that extracts features from the image and shrinks the image size. Reversely, in the decoder stage, the down-sampled image which is the output of the encoder is fed through a set of convolutions and up-sampling layers that eventually get the image back to the original input size with the same number of channels. The final output of the decoder is a pixel-level labelling of the original image. Semantic Segmentation Path (SSP) in Figure 4 shows this part of the fully convolutional network. In addition to the encoder-decoder architecture in U-Net, there are also skip-connections that bring the feature maps directly from an encoder stage to the corresponding decoder stage, i.e., the decoder stage that has the same image size of the encoder stage. These skip-connections improve the segmentation performance by re-accessing the early-stage features that are lost in the final output of the encoder due to down-sampling.

4.2. Four-Class Formulation

As mentioned earlier, prior approaches have considered either binary classification of HT, or a three-class formulation of the problem. Binary classification can detect only one type of text, and three-class formulation results in overlapping pixels to be assigned only to either HT or PT class, which hurts the performance. As such, we propose a four-class formulation of the segmentation task, and the fourth class, overlap, OV, models the pixels which belong to both HT and PT classes. This especially allows detecting the overlapping areas. To expand on Formula (1) for a four-class formulation, for a given document D, assuming there exist three classes as handwritten text HT, printed text PT, background BG, and overlap OV, and pixel p_i: $\forall p_i \in D : p_i(c) == True \quad if\ p_i \in c \ and \quad c \in \{HT, PT, BG, OV\}$.

Overlapping pixels are marked in yellow in the ground truth, e.g., Figure 3. Our four-class single-label classification leverages a Softmax activation function on the last layer, which means that only one of the outputs for each pixel will be set (Figure 4). Because the output image has three channels, if class OV is predicted, during a post-processing step we turn on pixels for both HT and PT channels, resulting in the yellow color in the output image. Besides the four-class formulation, we also explored three-class and multi-label formulations. In this scenario, instead of a Softmax activation, we performed Sigmoid activations per each class (i.e., three separate sigmoids). However, formulating the problem as a multi-label classification adds additional complexity and degrees of freedom, and irrelevant scenarios can happen, e.g., pixels with HT and BG may activate simultaneously. As such, the multi-label formulation did not perform on par with the four-class formulation.

4.3. Semantic Segmentation Path (SSP)

The semantic segmentation path (SSP) of our model leverages a U-Net based architecture, with down-sampling in the encoder stages (i.e., backbone) and up-sampling in the decoder stages. The U-net architecture works well in capturing high-level features of the image. In this architecture, the encoder and decoder apply a symmetrical architecture and similar number of stages. For example, in SSP, when the encoder goes through four down-sampling stages, i.e., the input image size changes from 256*256 to 16*16 (256→128→64→32→16), similarly, the decoder goes through four up-sampling stages, from 16*16 to 256*256, and the final output has the same pixel sizes as the original input image. For SSP, we explored a variety of

network sizes. As a baseline and for comparison, we implemented FCN-light [11, 28, 35]. We then improved on the SSP architecture by using VGG16 [31], InceptionV3 [34], and ResNet34 [15] as backbones of the SSP and observed improvement in the performance. In particular, ResNet34 and InceptionV3 backbones perform better compared to the prior work (FCN) as they have larger number of parameters to learn, and also the addition residual connections and different size convolutions allow to better carry over the low-level features of text to the later stages of the segmentation network. This observation also inspired us to introduce the FFP network, which similarly incorporates residual connections and without down-sampling.

4.4. Fine Feature Path (FFP)

The semantic segmentation path works well when there are distinct objects to segment. In this path, down-sampling layers are rapidly applied to the input image to capture high-level features and patterns. However, during this process, fine (i.e., low-level) features are lost. In our case, low-level features are also important due to the intertwined nature of printed and handwritten text. As such, we include a parallel path to SSP, namely a fine feature path (FFP) which does not perform down-sampling, but incorporates a convolution block with residual connections. Note that, at the same time that FFP is helping to capture fine features without down-sampling, FPP alone, i.e., without SPP that contains down-sampling, is not sufficient for text segmentation, as high-level features will be missing and the model will not be able to detect high-level patterns irrespective of their pixel locations in the image. For FFP in Figure 4, the fine feature block is repeated N_x times, and in our implementation $N_x = 4$. In addition, each stage of the FFP itself implements residual connections as it provides the flexibility to either bypass the block or use its output, and achieves better results as we review later in the paper. Similar architectures using residual blocks have shown improved performance in fine object segmentation, e.g., road segmentation [37]. Table 1 shows the FFP architecture for four stages ($N_x = 4$) and connections between layers and convolution sizes.

	Group	Layer type	Filter	Input(s)	Output(s)	Output size
Stage 1	G 1	Conv	$3 \times 3/64$	img_input	s1_g1_c_o	$256 \times 256 \times 64$
		BatchNorm	-	s1_g1_c_o	s1_g1_b_o	$256 \times 256 \times 64$
		ReLu	-	s1_g1_b_o	s1_g1_r_o	$256 \times 256 \times 64$
	G 2	Conv	$3 \times 3/64$	s1_g1_r_o	s1_g2_c_o	$256 \times 256 \times 64$
		BatchNorm	-	s1_g2_c_o	s1_g2_b_o	$256 \times 256 \times 64$
		Relu	-	s1_g2_b_o	s1_g2_r_o	$256 \times 256 \times 64$
		Concat	-	img_in, s1_g2_r_o	s1_o	$256 \times 256 \times 67$
Stage 2	G 1	Conv	$3 \times 3/64$	s1_o	s2_g1_c_o	$256 \times 256 \times 64$
		BatchNorm	-	s2_g1_c_o	s2_g1_b_o	$256 \times 256 \times 64$
		Relu	-	s2_g1_b_o	s2_g1_r_o	$256 \times 256 \times 64$
	G 2	Conv	$3 \times 3/64$	s2_g1_r_o	s2_g2_c_o	$256 \times 256 \times 64$
		BatchNorm	-	s2_g2_c_o	s2_g2_b_o	$256 \times 256 \times 64$
		ReLu	-	s2_g2_b_o	s2_g2_r_o	$256 \times 256 \times 64$
		Concat	-	s1_o, s2_g2_r_o	s2_o	$256 \times 256 \times 131$
Stage 3	G 1	Conv	$3 \times 3/64$	s2_o	s3_g1_c_o	$256 \times 256 \times 64$
		BatchNorm	-	s3_g1_c_o	s3_g1_b_o	$256 \times 256 \times 64$
		Relu	-	s3_g1_b_o	s3_g1_r_o	$256 \times 256 \times 64$
	G 2	Conv	$3 \times 3/64$	s3_g1_r_o	s3_g2_c_o	$256 \times 256 \times 64$
		BatchNorm	-	s3_g2_c_o	s3_g2_b_o	$256 \times 256 \times 64$
		ReLu	-	s3_g2_b_o	s3_g2_r_o	$256 \times 256 \times 64$
		Concat	-	s2_o, s3_g2_r_o	s3_o	$256 \times 256 \times 195$
Stage 4	G 1	Conv	$3 \times 3/64$	s3_o	s4_g1_c_o	$256 \times 256 \times 64$
		BatchNorm	-	s4_g1_c_o	s4_g1_b_o	$256 \times 256 \times 64$
		Relu	-	s4_g1_b_o	s4_g1_r_o	$256 \times 256 \times 64$
	G 2	Conv	$3 \times 3/64$	s4_g1_r_o	s4_g2_c_o	$256 \times 256 \times 64$
		BatchNorm	-	s4_g2_c_o	s4_g2_b_o	$256 \times 256 \times 64$
		ReLu	-	s4_g2_b_o	s4_g2_r_o	$256 \times 256 \times 64$
		Concat	-	s3_o, s4_g2_r_o	s4_o	$256 \times 256 \times 259$
Output	-	Conv	$1 \times 1/4$	s4_o	FFP_o	$256 \times 256 \times 4$

Table 1: The architecture of the Fine Feature Path (FFP). In our design, we use four stages (Stages 1-4) of the fine feature blocks. We include BatchNorm and ReLu activation after each convolution layer, and contrary to SSP, down-sampling layers (e.g., max pooling) are absent from FFP. The output of each stage is concatenated with its input to create residual connections.

4.5. Mixed Feature Model (MFM)

The mixed feature model (MFM) is the umbrella model that contains two parallel paths: SSP and FFP, as shown in Figure 4. The objective of MFM is to capture low-level features of the image, alongside its high-level features. The output of SSP and FFP are concatenated before performing the final layer convolution, which produces the output of MFM model. Additional details on the architecture, inputs, outputs, and convolution layer sizes of the MFM are available in the appendices.

4.6. CRF Post-Processing and CRF Heuristic

Prior research [11, 28, 35] has leveraged dense conditional Random Fields (CRFs) as a post-processing step to re-label pixels based on their adjacent pixels. During our architectural exploration, we observed that using CRF post-processing, although meant to improve the segmentation performance, in practice it actually hurts the segmentation performance in many cases as it aggressively re-labels pixels to a wrong class. One scenario is that due to the imbalanced nature of the number of pixels in each class, and background pixels being the dominant ones, many pixels are incorrectly annotated from HT or PT to BG, or from HT to PT, which is unfavourable. Because of this observation, we designed a heuristic for CRF post-processing to contain this unfavourable behaviour by only allowing the BG pixels to be relabelled to HT or PT pixels and not the other way around. As we will review in the experimentation section, this heuristic further improves the segmentation performance.

4.7. Loss Functions

Due to the nature of the scanned documents and the amount of text on each page, the number of background pixels (i.e., white blank pixels) is larger than the number of handwritten and printed pixels. This results in an imbalance class problem [38] with having the risk of predicting the majority of pixels as background while minimizing the loss value. As such, we investigated various loss functions and weight assignments to different classes in the loss function to assess the loss function's impact on the performance of the segmentation. Additionally, during this exploration, we noticed different loss functions achieve different IoU (Intersection over Union) scores. As such, we introduce a new loss function, Fusion Loss, to incorporate the benefits of different losses. In the following, we review different loss functions that we explored.

Cross-Entropy Loss. Multi-class cross-entropy loss is used for classification tasks with more than two classes and assumes for each data point only one of the classes can be ground truth class, i.e., multi-class single-label classification. The standard form of cross-entropy loss for a single data point for multi-class segmentation for M classes is defined as follows: $\mathcal{L}_{CE}(gt, pr) = -\sum_{m=1}^{M} gt \cdot \log(pr)$, with pr and gt being the prediction and ground truth respectively, and the final loss is the average of all the data point losses in a training set. Similarly, the weighted version (WCE) is calculated as $\mathcal{L}_{WCE}(gt, pr) = -\sum_{m=1}^{M} w_m \cdot gt \cdot \log(pr)$, where w_m is the weight of each class in the loss calculation.

Focal Loss. Focal loss [23] was introduced to address the class-imbalance problem for training in tasks for object detection. Focal loss aims to focus the learning on the incorrectly classified examples by applying a modulating term $(1 - pr)^{\gamma}$ to the cross-entropy loss. This scaling factor dynamically weighs down the contribution of easy and correctly classified samples, and allows the training loop to focus on harder and incorrectly classified samples. Focal loss is calculated as follows: $\mathcal{L}_{Focal}(gt, pr) = -\sum_{m=1}^{M} gt \cdot (1 - pr)^{\gamma} \log(pr)$, where γ is modulating/focusing factor, and we set $\gamma == 2$ as per the original paper. Similarly, the weighted version of the focal loss can be achieved as: $\mathcal{L}_{WF}(gt, pr) = -\sum_{m=1}^{M} gt \cdot \alpha_m \cdot (1 - pr)^{\gamma} \log(pr)$, where α_m is similar to w_m, assigning weights to each class such that: $\forall \alpha_m \mid 0 < \alpha_m < 1 \;\&\&\; \sum_{m=1}^{M} \alpha_m = 1$.

Dice Loss. Dice loss is defined as follows: $\mathcal{L}_{Dice}(precision, recall) = 1 - \frac{2}{M} \sum_{m=1}^{M} \frac{precision_m \cdot recall_m}{precision_m + recall_m}$, and intuitively speaking, it aims to maximize F-Score while minimizing the loss, i.e., $\mathcal{L}_{Dice} = 1 - F_{Score}$. Accordingly, the weighted version of the dice loss is defined as $\mathcal{L}_{WD}(precision, recall) = 1 - \frac{2}{M} \sum_{m=1}^{M} \frac{w_m \cdot precision_m \cdot recall_m}{precision_m + recall_m}$.

Fusion Loss. As we observed different loss functions perform adversely on different classes, we introduce a new loss targeted for maximizing the performance of all the classes. For example, dice loss performs better on the background class, as in its formulation, it aims to maximize F-Score. Because the majority of pixels belong to the background class, having higher values of correctly classified background pixels achieves a higher F-Score and lower loss values, but not necessarily higher IoU scores for PT and HT classes. Similarly, the weighted version of cross-entropy and focal losses focus on handwritten and printed classes. As such, with Fusion loss, we aim to combine the behavior of different losses, and we define the Fusion loss as the summation of the three weighted losses: $\mathcal{L}_{Fusion} = \mathcal{L}_{WF} + \mathcal{L}_{WCE} + \mathcal{L}_{WD}$

5. Experiments and Results

Evaluation Metric. Intersection over Union (IoU) is a standard metric that is generally used to measure the performance of a segmentation task [36], and in particular text segmentation [33, 18, 11, 35]. In this context, we use IoU to measure the pixel-level performance of the model output versus the ground truth. For class c, assuming TP_c is the correctly predicted pixels for that class, FP_c being the incorrectly predicted pixels for class c, and FN_c being the pixels that are incorrectly not predicted for class c, then intersection over union, IoU, for class c is calculated as: $IoU_c = \frac{TP_c}{TP_c + FP_c + FN_c}$. For each experiment, we calculate the IoU for all three classes, HT, PT, and BG. For the four-class formulation, the pixels that belong to the overlap (OV) class, are converted in a post-processing step for both HT and PT classes and participate in IoU calculations for both classes. We also calculate the mean IoU, which is the average of IoUs for the three classes: $IoU_{Mean} = \frac{IoU_{HT} + IoU_{PT} + IoU_{BG}}{3}$.

Experiments. We perform 50 epochs of training with a batch size of 8. For problem formulation, we use both three-class and four-class implementations. We experiment on two datasets, SignaTR6K and WGM-SYN [35]. FCN-light and WGM-MOD IoU values are as reported from [35] for three-class formulation which has been performed on the same dataset, WGM-SYN. However, for the SignaTR6K dataset, we re-train an FCN-based model for three-class formulation to make a fair comparison on the new dataset. We run experiments for a variety of architectures and in three post-processing configurations. We design experiments incrementally, i.e., adding one improvement at a time, to also allow us to understand and isolate the impact of each added improvement, i.e., ablation study. Due to space, we leave the table containing full list of experiment parameters and configurations in the appendices.

Experimented Architectures. We start with FCN-light which has approximately 295K parameters. This architecture is similar to prior research and acts as a baseline [11, 35]. Next, we improve the performance of FCN-light with four-class implementation. We then experiment with SSP architecture with three different backbones: VGG16, InceptionV3, and ResNet34. We also experiment with three variations of MFM which has both FFP and SSP, and with three SPP variations: VGG16, InceptionV3, and ResNet34. For our implementations, we use the Segmentation Models Library available in TensorFlow [16].

Post-Processing Configurations. There are three configurations that we experiment with: without post-processing, with CRF post-processing, and with CRFH post-processing. In without post-processing scenario, the IoU calculation is performed directly on the output of the model (FCN-light,

Formulation	Backbone	# Parameters	Loss function	IoU %				With CRF (IoU %)				With CRFH (IoU %)			
				PT	HT	BG	Mean	PT	HT	BG	Mean	PT	HT	BG	Mean
3-Class	**FCN-based [11, 35]**	∼295K	CE	62.56	88.09	98.40	83.02*	52.68	89.68	99.26	80.46	62.72	90.58	99.05	84.11
			Focal	62.34	88.00	98.45	82.93	44.60	84.86	99.28	76.25	62.57	90.83	99.21	84.21
			Dice	60.45	87.29	97.85	81.86	61.24	88.83	98.17	82.74	60.52	87.88	97.97	82.12
			Weighted CE	60.58	84.89	97.78	81.09	53.45	90.73	99.52	81.23	60.84	86.33	98.24	81.80
			Weighted Focal	61.25	85.74	98.02	81.67	44.27	85.77	99.50	76.51	61.55	87.42	98.58	82.52
			Weighted Dice	60.21	87.00	97.74	81.65	60.72	88.17	97.98	82.29	60.27	87.46	97.83	81.86
			Fusion	61.52	88.39	98.38	82.76	58.94	92.55	99.37	83.62	61.67	90.45	98.91	83.68
4-Class (Ours)	**FCN-based**	∼295K	CE	64.55	89.21	98.39	84.05	54.60	89.68	99.23	81.17	64.87	91.81	99.06	85.25
			Focal	64.10	88.86	98.32	83.76	46.64	86.01	99.26	77.30	64.34	91.65	99.11	85.03
			Dice	64.37	88.68	98.37	83.81	65.17	90.13	98.59	84.63	64.57	89.14	98.46	84.06
			Weighted CE	63.78	87.52	98.16	83.15	54.77	90.50	99.42	81.56	64.12	89.43	98.71	84.09
			Weighted Focal	63.68	87.71	98.19	83.20	48.18	87.10	99.45	78.24	64.05	89.72	98.80	84.19
			Weighted Dice	64.21	88.57	98.30	83.69	65.08	90.10	98.53	84.57	64.44	89.06	98.39	83.96
			Fusion	64.68	88.48	98.33	83.83	59.83	91.77	99.28	83.63	65.00	90.72	98.91	84.87
	MFM (FFP + SSP) - InceptionV3	∼30M	CE	73.10	92.66	98.77	88.18	63.48	92.89	99.55	85.31	73.05	94.89	99.36	**89.10**
			Focal	72.80	92.50	98.75	88.01	57.47	90.58	99.54	82.53	72.77	94.74	99.35	88.95
			Dice	72.56	92.20	98.70	87.82	72.38	93.60	99.00	88.33	72.52	94.73	99.37	88.87
			Weighted CE	72.66	91.90	98.54	87.70	62.65	93.04	**99.62**	85.10	72.63	93.31	98.94	88.29
			Weighted Focal	72.55	92.13	98.62	87.77	59.35	91.64	99.59	83.53	72.50	93.77	99.07	88.45
			Weighted Dice	72.59	92.31	98.70	87.87	72.60	94.00	99.07	88.56	72.54	94.60	99.32	88.82
			Fusion	72.55	92.25	98.71	87.83	65.57	93.49	99.53	86.19	72.49	94.62	99.35	88.82
	MFM (FFP + SSP) - ResNet34	∼24M	CE	72.81	92.56	98.78	88.05	63.04	92.94	99.55	85.17	72.75	**94.93**	99.39	89.02
			Focal	73.04	92.46	98.75	88.08	53.02	89.04	99.55	80.54	73.00	94.75	99.35	89.03
			Dice	72.96	92.38	98.72	88.02	73.16	93.35	98.93	88.48	72.93	94.79	99.36	89.03
			Weighted CE	72.96	91.96	98.69	87.87	64.49	92.47	99.56	85.51	72.90	94.19	99.27	88.79
			Weighted Focal	73.18	92.10	98.63	87.97	54.96	89.71	99.60	81.42	73.16	93.72	99.06	88.65
			Weighted Dice	72.78	92.32	98.71	87.94	72.95	93.66	99.00	88.53	72.75	94.67	99.34	88.92
			Fusion	**73.26**	92.45	98.73	88.15	68.38	94.85	99.56	87.60	73.21	94.59	99.31	89.04

Table 2: IoU performance (%) on SignaTR6K dataset. The maximum value of a column (i.e., class) is underlined, and the overall maximum of a class with different post-processing is denoted in bold and underlined. For example, the best mean IoU for the SignaTR6K dataset is for CE loss, with CRFH, and MFM-InceptionV3 architecture at **89.10**. The best performing configuration of prior work, i.e., excluding results for Fusion loss and CRFH, marked with (*), is 83.02.

SSP, and MFM). For CRF post-processing, we perform post processing by allowing all classes to be relabeled. However, in CRF post-processing with heuristic (CRFH), as explained in Section 4.6, we only allow the background class pixels (BG) to be relabeled to HT and PT classes.

Weight Initialization. For FCN-light and SSP models, model weights start from their initial random values at the beginning of the training. We train MFM configurations at last to reuse the weights from SSP configurations. As such, for the MFM trainings, we apply transfer learning and use the weights from corresponding previously trained SSP. For example, for MFM (FFP+SSP) with SSP as ResNet34 backbone, we initialize its SSP path with the available weights from SSP - ResNet34. Lastly, as we have aimed to fix the seeds to allow repeatable IoU results, however, there is still an inherent non-determinism of execution on GPUs. As such, we have run our experiments multiple times to confirm the IoU value improvements for each configuration.

Results. Table 2 show the IoU values for SignaTR6K dataset. Overall trends of the results show that going from the three-class formulation to the four-class formulation improves IoUs. Additionally, using larger model backbones generally improves the segmentation performance. Among all the model architectures, the ResNet34 and InceptionV3 backbones achieve the highest performance, which we contribute to their residual connections and different size convolutions as they can better incorporate fine features from the image. We summarize the trends in the results here and the rest are available in the appendicitises.

- Prior work [11, 35] which implements the three-class formulation of HT and PT segmentation generally achieves the lowest performance. Going from three-class formulation to four-class formulation with the same backbone, i.e., FCN-light, with the same number of model parameters and WCE loss, improves the average IoU values by 8.0% (50→54.02) for WGM-SYN, and 2.6% (81.09→83.15) for SignaTR6K datasets.
- Applying CRF post-processing generally degrades the results. In our research, we observe that CRF post processing is dataset dependent and decreases the performance of segmentation in some cases. CRF post-processing relabels aggressively and incorrectly converts HT and PT pixels to background ones, or OV pixels to PT ones. For example, Figure 5i illustrates that how OV pixels are wrongly relabeled to PT class by CRF post-processing. Contrary to CRF post-processing, our CRF heuristic generally improves the IoU values. For example, for the SignaTR6K dataset, for FCN-light with four-class implementation and CE loss, CRFH improves HT IoUs by 2.9% (89.21→91.81).
- Moving from FCN-light architecture to larger models, i.e., SSP and MFM models, generally improves the results, except for the VGG16 backbone. For VGG16, we rationalize that having a deep network without residual connections or different size convolutions, which exist in ResNet34

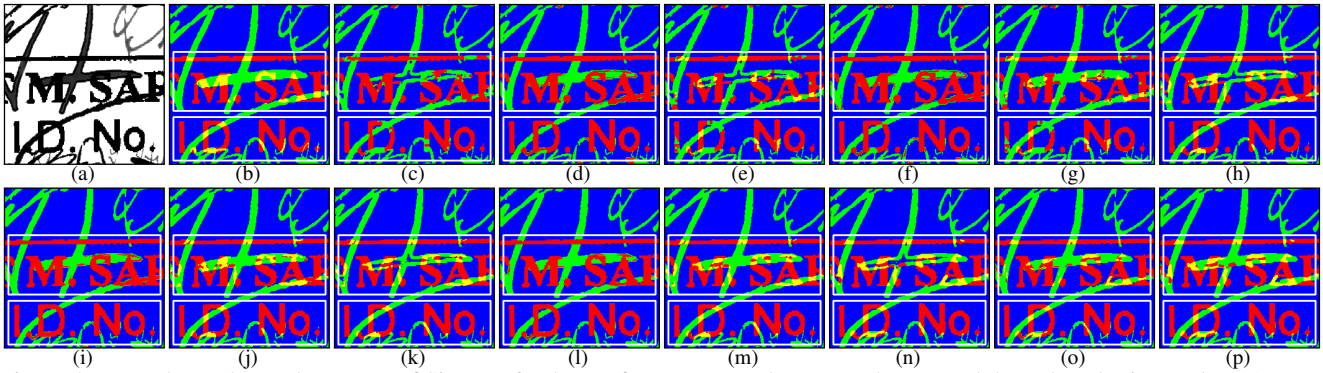

Figure 5: Example results on the test set of SignaTR6K dataset for our approach compared to ground through and prior works. (a) Input image; (b) Ground truth; (c) & (d) 3-class FCN-based [11, 35] with CE loss without (c) and with (d) CRF post-processing; (e), (f), & (g) Our FCN-based 4-class formulation with CE loss without CRF (e), with CRF (f), and with CRFH (g); (h), (i), & (j) SSP-ResNet34 with CE loss without CRF (h), with CRF (i), and with CRFH (j); (k), (l), & (m) MFM-ResNet34 with CE loss without CRF (k), with CRF (l), and with CRFH (m); (n), (o), & (p) MFM-ResNet34 with Fusion loss without CRF (n), with CRF (o), and with CRFH (p);

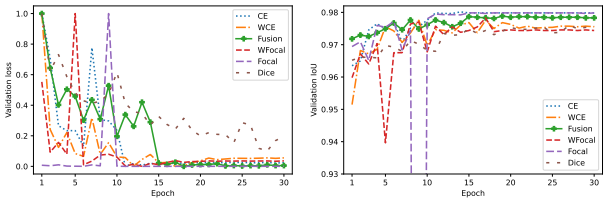

(a) Validation set losses (b) Validation set IoUs

Figure 6: Convergence speed of different loss functions and normalized loss values on the validation set of the SignaTR6K dataset.

and InceptionV3 architecture, would hurt the model in capturing fine features. In addition, we observe that adding the FFP helps to improve the performance of the VGG model as we compare SSP and MFM performance values for both datasets. This also confirms the FFP's ability to capture low-level features that are missed in the SSP path.

- MFM model with ResNet34 and InceptionV3 backbones generally achieve the best results. MFM-ResNet34 with Fusion loss and CRFH achieves the best result for the WGM-SYN dataset (58.93%), and MFM-InceptionV3 with CE loss and CRFH achieves the best mean IoUs for the SignaTR6K dataset (89.10%). Overall, the best-performing model from our designs improves on the mean IoU performance of the best-performing prior work [35] by 17.9% (50→58.93) and 7.3% (83.02→89.10) for WGM-SYN and SignaTR6K datasets, respectively. More results on the WGM-SYN dataset and our approach limitations are available in the appendices.

Loss Functions. We also perform analysis to confirm the stability and convergence of the Fusion loss compared to other losses. Figures 6a and 6b compare different loss functions on the validation set of the SignaTR6K dataset. In Figure 6a, we observe Fusion loss is generally stable while converging to its minimum loss. Additionally, in Figure 6b, we observe Fusion loss reaches its maximum IoU around Epoch 15, generally faster than the majority of losses and stays close to the maximum IoU values on the validation set. We also note that the maximum IoU on the validation set, Focal and CE losses, does not imply the best performance on the test set. Overall, Fusion loss shows a stable behavior and achieves a better performance on the test set, whereas, for comparison, Focal loss shows instability at some epochs during the training.

Visual Comparison. Figure 5 shows sample model outputs for SignaTR6K dataset, and two rectangle regions of interest are marked to show the differences between different models. Figure 5b shows the ground truth, and we can visually observe a trend that the performance on the regions of interest improves from Figure 5c to Figure 5p. It is also visually noticeable that CRF post-processing aggressively retables pixels (5i), and CRFH generally improves the results. Additional visual comparisons on WGM-SYN dataset are available in the appendices.

6. Conclusion

Handwritten text (HT) and printed text (PT) segmentation has been a crucial problem for digitization and understanding of scanned documents. The problem becomes even more challenging due to the overlapping of different types of text. In this research, we presented a new open-source dataset, SignaTR6K, that has high-quality and manual pixel-level annotations, and is sourced from original documents from legal domain. Additionally, we introduced a four-class formulation and proposed a new architecture for the segmentation task. With four-class formulation and incorporation of fine feature path (FFP) and semantic segmentation path (SSP), we introduced a new architecture, MFM, that incorporates both high-level and low-level features and improves on the text segmentation performance. We also introduced a CRF-based post-processing heuristic (CRFH) that further improves the model output, and included a new loss function, namely Fusion loss, that combines the advantages of different loss functions and achieves faster convergence and higher stability compared to the most of

the evaluated losses. In summary, our designs outperform the prior work in mean IoU scores by 17.9% and 7.3% on WGM-SYN and SignaTR6K datasets, respectively.

References

[1] ABBYY FineReader PDF. https://pdf.abbyy.com/. Accessed: 2023-01-21.

[2] Amazon Textract. https://aws.amazon.com/textract/. Accessed: 2023-01-21.

[3] RIMES. http://www.a2ialab.com/doku.php?id=rimesdatabase:start. Inaccessible: 2023-01-23.

[4] Scanned Questionnaire. https://github.com/jottue/HTSNet. Accessed: 2023-01-23.

[5] Tesseract. https://github.com/tesseract-ocr/tesseract. Accessed: 2023-01-21.

[6] Thomson Reuters Legal Content Services. https://www.thomsonreuters.com/en/products-services/legal.html. Accessed: 2023-01-21.

[7] VOTT. https://github.com/microsoft/VoTT. Accessed: 2023-01-29.

[8] Wiedergutmachung. https://www.fiz-karlsruhe.de/en/forschung/wiedergutmachung. Accessed: 2023-01-29.

[9] Apostolos Antonacopoulos, David Bridson, Christos Papadopoulos, and Stefan Pletschacher. A realistic dataset for performance evaluation of document layout analysis. In *2009 10th International Conference on Document Analysis and Recognition*, pages 296–300. IEEE, 2009.

[10] Dibyajyoti Dhar, Avishek Garain, Pawan Kumar Singh, and Ram Sarkar. Hp_docpres: A method for classifying printed and handwritten texts in doctor's prescription. *Multimedia Tools and Applications*, 80(7):9779–9812, 2021.

[11] Nicolas Dutly, Fouad Slimane, and Rolf Ingold. Phti-ws: a printed and handwritten text identification web service based on fcn and crf post-processing. In *2019 International Conference on Document Analysis and Recognition Workshops (ICDARW)*, volume 2, pages 20–25. IEEE, 2019.

[12] Jürgen Franke and Matthias Oberlander. Writing style detection by statistical combination of classifiers in form reader applications. In *Proceedings of 2nd International Conference on Document Analysis and Recognition (ICDAR'93)*, pages 581–584. IEEE, 1993.

[13] Bala Mallikarjunarao Garlapati and Srinivasa Rao Chalamala. A system for handwritten and printed text classification. In *2017 UKSim-AMSS 19th International Conference on Computer Modelling & Simulation (UKSim)*, pages 50–54. IEEE, 2017.

[14] Greg Hamerly and Charles Elkan. Learning the k in k-means. *Advances in neural information processing systems*, 16, 2003.

[15] Kaiming He, Xiangyu Zhang, Shaoqing Ren, and Jian Sun. Deep residual learning for image recognition. In *Proceedings of the IEEE conference on computer vision and pattern recognition*, pages 770–778, 2016.

[16] Pavel Iakubovskii. Segmentation models. https://github.com/qubvel/segmentation_models, 2019.

[17] Noman Islam, Zeeshan Islam, and Nazia Noor. A survey on optical character recognition system. *arXiv preprint arXiv:1710.05703*, 2017.

[18] Junho Jo, Hyung Il Koo, Jae Woong Soh, and Nam Ik Cho. Handwritten text segmentation via end-to-end learning of convolutional neural networks. *Multimedia Tools and Applications*, 79(43):32137–32150, 2020.

[19] Celso AML Junior, Matheus Henrique Marques da Silva, Byron Leite Dantas Bezerra, Bruno José Torres Fernandes, and Donato Impedovo. Fcn+ rl: a fully convolutional network followed by refinement layers to offline handwritten signature segmentation. In *2020 International Joint Conference on Neural Networks (IJCNN)*, pages 1–7. IEEE, 2020.

[20] R Kandan, Nirup Kumar Reddy, KR Arvind, and AG Ramakrishnan. A robust two level classification algorithm for text localization in documents. In *Advances in Visual Computing: Third International Symposium, ISVC 2007, Lake Tahoe, NV, USA, November 26-28, 2007, Proceedings, Part II 3*, pages 96–105. Springer, 2007.

[21] Florian Kleber, Stefan Fiel, Markus Diem, and Robert Sablatnig. Cvl-database: An off-line database for writer retrieval, writer identification and word spotting. In *2013 12th international conference on document analysis and recognition*, pages 560–564. IEEE, 2013.

[22] Xiao-Hui Li, Fei Yin, and Cheng-Lin Liu. Printed/handwritten texts and graphics separation in complex documents using conditional random fields. In *2018 13th IAPR International Workshop on Document Analysis Systems (DAS)*, pages 145–150. IEEE, 2018.

[23] Tsung-Yi Lin, Priya Goyal, Ross Girshick, Kaiming He, and Piotr Dollár. Focal loss for dense object detection. In *Proceedings of the IEEE international conference on computer vision*, pages 2980–2988, 2017.

[24] Jonathan Long, Evan Shelhamer, and Trevor Darrell. Fully convolutional networks for semantic segmentation. In *Proceedings of the IEEE conference on computer vision and pattern recognition*, pages 3431–3440, 2015.

[25] U-V Marti and Horst Bunke. The iam-database: an english sentence database for offline handwriting recognition. *International Journal on Document Analysis and Recognition*, 5(1):39–46, 2002.

[26] Milda Norkute, Nadja Herger, Leszek Michalak, Andrew Mulder, and Sally Gao. Towards explainable ai: Assessing the usefulness and impact of added explainability features in legal document summarization. In *Extended Abstracts of the 2021 CHI Conference on Human Factors in Computing Systems*, pages 1–7, 2021.

[27] Xujun Peng, Srirangaraj Setlur, Venu Govindaraju, and Ramachandrula Sitaram. Handwritten text separation from annotated machine printed documents using markov random fields. *International Journal on Document Analysis and Recognition (IJDAR)*, 16(1):1–16, 2013.

[28] Anastasia Prikhodina. Handwritten and printed text separation for historical documents. 2021.

[29] Olaf Ronneberger, Philipp Fischer, and Thomas Brox. U-net: Convolutional networks for biomedical image segmentation. In *International Conference on Medical image computing and computer-assisted intervention*, pages 234–241. Springer, 2015.

[30] Mathias Seuret, Marcus Liwicki, and Rolf Ingold. Pixel level handwritten and printed content discrimination in scanned documents. In *2014 14th International Conference on Frontiers in Handwriting Recognition*, pages 423–428. IEEE, 2014.

[31] Karen Simonyan and Andrew Zisserman. Very deep convolutional networks for large-scale image recognition. *arXiv preprint arXiv:1409.1556*, 2014.

[32] Stavroula Skylaki, Ali Oskooei, Omar Bari, Nadja Herger, and Zac Kriegman. Named entity recognition in the legal domain using a pointer generator network. *arXiv preprint arXiv:2012.09936*, 2020.

[33] Nishant Subramani, Alexandre Matton, Malcolm Greaves, and Adrian Lam. A survey of deep learning approaches for ocr and document understanding. *arXiv preprint arXiv:2011.13534*, 2020.

[34] Christian Szegedy, Vincent Vanhoucke, Sergey Ioffe, Jon Shlens, and Zbigniew Wojna. Rethinking the inception architecture for computer vision. In *Proceedings of the IEEE conference on computer vision and pattern recognition*, pages 2818–2826, 2016.

[35] Mahsa Vafaie, Oleksandra Bruns, Nastasja Pilz, Jörg Waitelonis, and Harald Sack. Handwritten and printed text identification in historical archival documents. In *Archiving Conference*, volume 19, pages 15–20. Society for Imaging Science and Technology, 2022.

[36] Zhaobin Wang, E Wang, and Ying Zhu. Image segmentation evaluation: a survey of methods. *Artificial Intelligence Review*, 53:5637–5674, 2020.

[37] Zhengxin Zhang, Qingjie Liu, and Yunhong Wang. Road extraction by deep residual u-net. *IEEE Geoscience and Remote Sensing Letters*, 15(5):749–753, 2018.

[38] Zhi-Hua Zhou and Xu-Ying Liu. Training cost-sensitive neural networks with methods addressing the class imbalance problem. *IEEE Transactions on knowledge and data engineering*, 18(1):63–77, 2005.

Appendices

In the appendices, we review some additional background, architecture details, and results.

A. Additional Background and Related Work

A.1. Scope

Converting hard-copy documents, or microfilms in case of archival and historical documents [35], to their digital format has been the focus of the computer vision research community, and multiple approaches have been proposed for this purpose [17, 33]. For a variety of reasons, such as document understanding, paper documents in different domains, such as books, archival documents, medical records, legal documents, survey forms, etc., are converted to their digital format through optical character recognition (OCR). Because of the high demand in the digitization of documents, several commercial and open-source OCR engines such as Amazon's Textract [2], Tessaract [5], and ABBYY FineReader [1] have been available for some time. These tools significantly speed up the automatic digitization of documents at scale. However, due to the variety in types of documents, their structure, overlaying handwritten and printed text, and also the poor quality of original documents and their scanned version in the case of historical documents, the quality of OCR tools can degrade in the digitization process [35, 13]. As such, our approach aims to tackle and improve the quality of text segmentation to benefit the downstream tasks.

A.2. Models

Parts of this section were presented in the main text, and in the following, we review a more comprehensive version. Prior work has applied several methods for handwritten and printed text segmentation. Early approaches [12, 20] formulated the problem as a binary classification task, with KNN and SVM, and used connected component (CC) (i.e., group of pixels) based on different sets of features to decide whether a CC is HT or MT text. The features include geometric features of CCs such as their heights, widths, and the spread between CCs [12] and geometric-invariant ones such as invariant moments[20]. More recently, Li et al. [22] applied conditional random fields (CRFs), with formulating both unary and pair-wise potentials for adjacent connected components by leveraging convolutional neural networks (CNNs) architecture for the separation of CCs. The main drawback with CC-based approaches is that it assigns a single class for the entire component, instead of a pixel-level class assignment, and also fails to detect overlapping regions as the entire connected component is assigned to either HT or PT class.

Due to connected components drawbacks, pixel-level segmentation methods were proposed that leverage Markov random fields (MRFs) [27]. Authors of [27] apply both patch-level and pixel-level classification for PT and HT segmentation with are initially identified using G-means based (a modified version of k-means [14]) classification followed by a relabeling step based on MRFs. Seuret et al. [30] classified the foreground pixels as printed or handwritten text by using an MLP architecture with two fully-connected hidden units. The MLP is followed by a post-processing step that corrects probable mistakes based on adjacent pixels.

As the encoder-decoder architectures have proven to perform quite well in object segmentation [29], more recent works [18, 11, 28, 35] have generally applied a U-Net based architecture [29] for HT and PT segmentation. This architecture consists of an encoder-decoder architecture, similar to SSP in Figures 4 and 8. Jo et al [18] levered a U-net architecture to perform binary classification of handwritten text. Similarly, authors in several research [11, 28, 35] leveraged a fully convolutional network (FCN) for classification of three classes: handwritten (HT), printed (PT), background (BG). The approaches are tuned for different applications such as web-based services [11] and understanding of historical documents [28, 35]. The approaches also apply a conditional random field (CRF) post-processing step to relabel pixels based on their adjacent majority pixels. These approaches perform a three-class formulation of text segmentation, which assigns the overlapping pixels to only one of HT or PT classes and the CRF post-processing often performs aggressive re-labelling that degrades the segmentation performance [28, 35].

A.2.1 WGM-SYN Dataset

Besides the SignaTR6K dataset, we also performed an evaluation on WGM-SYN dataset [35]. This dataset contains a subset of historical and archival records and documents from the "Pilotprojekt zur Wiedergutmachung" archive [8]. The dataset is collected from forms, typewritten certificates, decelerations, and testimonies with different layouts, both in color and gray-scale. Then, the documents are manually annotated for different types of text with VOTT3 [7]. This process results in 319 images of handwritten and 767 images of machine-written text both from microfilm and document scans. Finally, after some preprocessing, noise removal, and binarization steps, data synthesis approaches adopted from [18] are applied. This approach results in the final training, validation, and testing sizes of 3335, 430, and 430, respectively. Each data sample has a gray-scale image crop of size 256*256 pixels containing handwritten and machine-written text, and a color-coded label with handwritten as green, machine-written as red, and background as blue. Figure 7 illustrates an example from the WGM-SYN dataset.

	Group	Layer type	Filter	Input(s)	Output(s)	Output size
Input	_	Input	_	img_input	i_o	$256 \times 256 \times 3$
Fine Feature Path	G 1	FFP	_	i_o	FFP_o	$256 \times 256 \times 4$
		BatchNorm	_	FFP_o	g1_b_o	$256 \times 256 \times 4$
		ReLu	_	g1_b_o	g1_r_o	$256 \times 256 \times 4$
Semantic Segmentation Path	G 2	SSP	_	i_o	SSP_o	$256 \times 256 \times 4$
		BatchNorm	_	SSP_o	g2_b_o	$256 \times 256 \times 4$
		ReLu	_	g2_b_o	g2_r_o	$256 \times 256 \times 4$
Concatenation	G 3	Concat	_	g1_r_o, g2_r_o	g3_cc_o	$256 \times 256 \times 8$
		Conv	$1 \times 1/4$	g3_cc_o	g3_cv_o	$256 \times 256 \times 4$
		Softmax	_	g3_cv_o	g3_s_o	$256 \times 256 \times 4$
Output	_	Output	_	g3_s_o	MFM_{output}	$256 \times 256 \times 4$

Table 3: The architecture and connections of the high-level model, Mixed Feature Model (MFM).

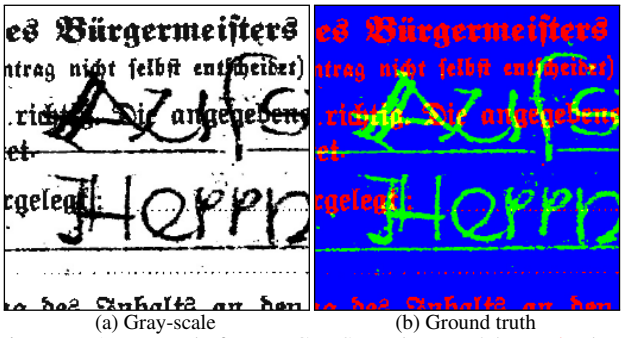

(a) Gray-scale (b) Ground truth

Figure 7: An example from WGM-SYN dataset [35]. Red: class PT, printed, Green: class HT, handwritten, and Blue: class BG, background.

B. Architecture

We provide additional details on the overall architecture of MFM in Table 3 and Figure 8. Table 3 shows the stages and connections for MFM, and Figure 8 shows more details of SSP and FFP blocks.

C. Additional Experiments and Results

C.1. Experiments Configurations

Table 4 provides additional details on the experimented configurations. For learning rate (LR), we start with the initial value of 0.001 and divide by ten if there is no improvement in validation loss values after four epochs.

C.2. Additional Results

Tables 5 and 6 show the IoU values for WMG-SYN and SignaTR6K datasets, respectively. Overall trends of the results show that going from the three-class formulation to the four-class formulation improves the IoU values. Additionally, using larger model backbones generally improves the segmentation performance. Among all the model architectures, the ResNet34 backbone achieves the highest performance, which we contribute to its residual connections as they can better incorporate the finer features from the image.

Parameter	Details
Training epochs	50
Batch size	8
Loss functions	Cross-entropy, WCE, Focal, WF, Dice, WD, and Fusion
Weighted Loss functions weights	3-class: [PT, HT, BG] = [0.4, 0.5, 0.1], 4-class: [PT, HT, BG, OV]=[0.3, 0.3, 0.1, 0.3]
Initial learning rate (LR)	0.001
LR schedule	LR = LR/10 if no reduction in validation loss for 4 epochs.
Initial weights	FCN: None; SSP: None; MFM: SSP initialized with prior training weights
Optimizer	Adam
SignaTR6K	Training: 5169; Validation: 530; Test: 558
WGM-SYN	Training: 3335; Validation: 430; Test: 430
Problem formulation	three-class and four-class
Architecture variations	WGM-MOD & FCN-light (3-class); FCN-light (4-class); SSP (VGG16, InceptionV3, and Resnet34); MFM (VGG16, InceptionV3, and ResNet34)

Table 4: Experimentation parameters.

C.3. Limitations

Limitations of our approach compared to the prior work include the complexity and training cost. Our MFM model is larger when compared to FCN-light, and requires larger GPU memory sizes to train, and the training takes longer. However, we believe some of the limitations on training time can be offset through weight transfer from SPP models to MFM ones. Additionally, although our approach outperforms prior work on the WGM-SYN dataset, we observe that the mean IoU performance is lower compared to the

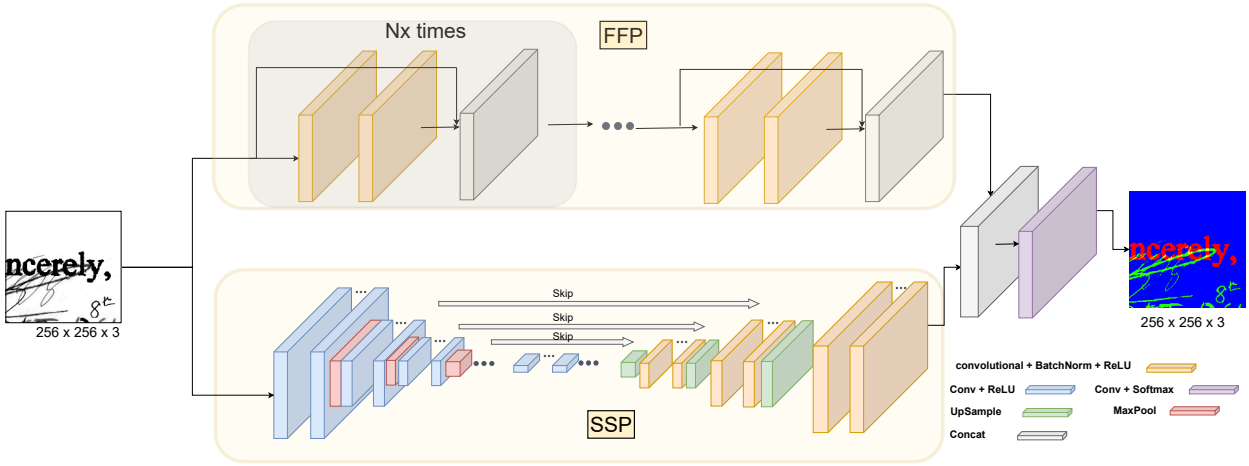

Figure 8: Our architecture proposal is to use the fine feature path in parallel to the U-Net architecture (SSP) to capture low-level features of the image, as the U-Net captures high-level features with condensing and expanding. For SSP, the three dots in the middle show that different sets of encoders and decoders can be applied. As such, we explored various backbones, such as FCN-light, VGG16, InceptionV3, and ResNet34.

SignaTR6K dataset. This implies that our approach might not perform as well in the cases where the original documents have lower quality or the scanning process is not quite well, in this example historical documents.

C.4. Visual Comparisons

Figures 9 and 10 provide additional visual comparisons for WGM-SYN and SignaTR6K datasets. Figures 9b and 10b show the ground truth, and we can visually observe a trend that the performance on the HT and PT overlapping regions improves from (c) to (p). It is also visually noticeable that CRF post-processing aggressively relabels pixels, and CRFH generally improves the results.

C.5. Dataset Availability

We have included some samples from the SignaTR6K dataset in the supplementary material, and the entire dataset will be available upon the acceptance of the paper.

Formulation	Backbone	# Parameters	Loss function	IoU %				With CRF (IoU %)				With CRFH (IoU %)			
				PT	HT	BG	Mean	PT	HT	BG	Mean	PT	HT	BG	Mean
3-Class	**FCN-light** [11]	∼295K	Weighted CE	24.00	26.00	72.00	41.00	11.00	23.00	72.00	36.00	-	-	-	-
	WGM-MOD [35]	∼295K	Weighted CE	42.00	36.00	74.00	50.00*	41.00	32.00	74.00	49.00	-	-	-	-
4-Class (Ours)	**FCN-light**	∼295K	CE	46.49	41.98	73.77	54.08	38.95	29.35	73.92	47.41	46.57	41.59	73.87	54.01
			Focal	46.02	42.01	73.80	53.95	32.96	24.50	74.00	43.82	46.11	41.23	73.98	53.77
			Dice	48.01	47.28	71.22	55.55	48.59	48.48	71.22	56.10	48.07	47.79	71.29	55.72
			Weighted CE	46.07	42.18	73.82	54.02	40.54	30.07	73.98	48.20	46.31	41.68	73.95	53.98
			Weighted Focal	43.71	41.77	73.95	53.14	32.67	24.40	74.07	43.71	44.06	41.12	74.11	53.10
			Weighted Dice	47.97	47.22	71.02	55.40	48.69	48.34	71.02	56.02	48.04	47.70	71.10	55.61
			Fusion	48.12	47.25	71.93	55.77	46.34	44.25	71.86	54.15	48.19	47.89	72.38	56.15
	SSP - VGG16	∼24M	CE	35.14	32.40	73.96	47.17	30.97	19.14	73.88	41.33	35.21	32.08	74.13	47.14
			Focal	34.56	32.22	74.02	46.93	29.11	19.42	73.91	40.81	34.67	31.79	74.22	46.89
			Dice	40.64	39.64	71.13	50.47	43.30	40.16	71.21	51.55	40.81	40.25	71.25	50.77
			Weighted CE	35.73	33.44	74.43	47.87	32.00	20.70	74.12	42.28	35.93	32.95	74.65	47.84
			Weighted Focal	34.90	34.35	74.36	47.87	29.18	20.72	74.06	41.32	35.11	33.80	74.56	47.82
			Weighted Dice	41.80	40.64	70.67	51.03	44.14	41.39	70.70	52.07	42.52	41.19	70.97	51.56
			Fusion	39.99	39.56	72.31	50.62	35.39	27.93	72.35	45.22	40.10	39.94	72.63	50.89
	MFM (FFP + SSP) - VGG16	∼24M	CE	42.41	40.41	73.76	52.19	33.84	25.74	73.97	44.52	42.44	39.13	74.09	51.89
			Focal	41.61	39.11	73.77	51.50	30.85	23.13	74.04	42.67	41.64	37.74	74.13	51.17
			Dice	21.33	19.96	80.50	40.59	23.39	21.96	80.00	41.78	21.35	20.00	80.51	40.62
			Weighted CE	42.60	40.83	73.85	52.43	34.88	25.90	74.03	44.94	42.63	39.61	74.16	52.13
			Weighted Focal	42.22	40.83	73.85	52.30	30.79	23.74	74.10	42.88	42.25	39.51	74.18	51.98
			Weighted Dice	28.51	27.57	76.39	44.16	30.89	29.32	75.67	45.29	28.70	27.87	76.37	44.31
			Fusion	44.80	45.64	72.10	54.18	40.77	36.92	72.00	49.90	44.88	44.67	72.86	54.14
	SSP - InceptionV3	∼30M	CE	49.54	42.13	74.10	55.26	42.80	33.23	74.17	50.07	49.56	41.24	74.34	55.05
			Focal	47.49	42.03	73.94	54.49	35.24	26.26	74.11	45.20	47.54	40.95	74.22	54.24
			Dice	51.22	49.71	71.39	57.44	51.87	**52.01**	71.38	58.42	51.32	50.42	71.56	57.77
			Weighted CE	48.82	41.55	74.34	54.90	43.84	32.55	74.26	50.22	48.92	40.63	74.59	54.71
			Weighted Focal	45.06	40.39	74.19	53.21	34.27	24.89	74.29	44.48	45.27	39.25	74.52	53.01
			Weighted Dice	51.35	49.58	71.00	57.31	52.04	51.12	71.03	58.06	51.45	50.32	71.15	57.64
			Fusion	51.29	49.51	71.71	57.50	48.82	46.27	71.78	55.62	51.37	50.46	72.15	58.00
	MFM (FFP + SSP) - InceptionV3	∼30M	CE	52.51	44.09	73.91	56.84	46.03	35.94	74.21	52.06	52.55	42.17	74.35	56.36
			Focal	51.56	43.74	73.89	56.40	35.89	27.15	74.41	45.82	51.63	41.74	74.43	55.93
			Dice	20.91	19.28	81.52	40.57	25.51	24.61	79.94	43.35	20.92	19.29	81.54	40.58
			Weighted CE	51.58	43.72	73.95	56.42	44.78	34.04	74.32	51.05	51.64	41.85	74.40	55.96
			Weighted Focal	51.01	43.62	73.89	56.18	35.76	26.60	74.22	45.53	51.08	41.60	74.35	55.68
			Weighted Dice	22.30	21.25	80.73	41.42	29.11	29.48	77.97	45.52	22.32	21.26	80.74	41.44
			Fusion	53.22	51.25	71.84	58.77	50.05	48.83	72.03	56.97	**53.32**	49.83	72.72	58.62
	SSP - ResNet34	∼24M	CE	51.94	43.74	73.94	56.54	45.76	35.32	74.18	51.75	51.98	43.13	74.08	56.39
			Focal	50.99	43.45	73.93	56.12	35.76	27.78	74.33	45.96	50.99	42.34	74.19	55.84
			Dice	20.88	19.54	**82.08**	40.83	22.00	20.83	81.89	41.57	20.88	19.55	**82.08**	40.83
			Weighted CE	51.45	43.27	74.03	56.25	45.76	35.01	74.13	51.63	51.43	42.55	74.20	56.06
			Weighted Focal	50.16	43.02	73.97	55.72	35.64	27.54	74.25	45.81	50.18	41.89	74.25	55.44
			Weighted Dice	52.04	50.75	70.97	57.92	52.35	51.94	71.00	58.43	52.09	51.25	71.07	58.14
			Fusion	52.58	50.69	71.77	58.35	50.19	48.91	71.94	57.01	52.60	51.86	72.19	58.88
	MFM (FFP + SSP) - ReNet34	∼24M	CE	52.40	44.02	73.91	56.78	47.52	36.40	74.12	52.68	52.43	42.12	74.34	56.30
			Focal	51.95	43.98	73.89	56.61	36.73	27.17	74.31	46.07	51.90	41.99	74.33	56.08
			Dice	29.68	29.43	77.06	45.39	31.62	25.39	75.15	44.05	29.84	29.63	77.07	45.52
			Weighted CE	52.63	44.12	73.94	56.90	47.60	37.25	74.12	52.99	52.56	42.22	74.36	56.38
			Weighted Focal	51.68	43.95	73.90	56.51	35.73	27.22	74.30	45.75	51.72	41.98	74.34	56.01
			Weighted Dice	51.44	50.60	71.96	58.00	52.97	51.42	71.90	58.76	51.54	49.37	72.75	57.89
			Fusion	52.99	51.72	71.69	58.80	51.15	50.79	71.83	57.92	53.01	51.29	72.49	**58.93**

Table 5: IoU performance (%) on WGM dataset [35]. The maximum value of a column (i.e., class) is underlined. The overall maximum of a class with different post-processing is marked in bold and underlined. For example, the best mean IoU for the WGM-SYN dataset is for Fusion loss, with CRFH, and MFM-ResNet34 architecture at **58.93**. The best performing configuration of prior work, marked with (*), is 50.00.

Formulation	Backbone	# Parameters	Loss function	IoU %				With CRF (IoU %)				With CRFH (IoU %)			
				PT	HT	BG	Mean	PT	HT	BG	Mean	PT	HT	BG	Mean
3-Class	**FCN-based [11, 35]**	∼295K	CE	62.56	88.09	98.40	83.02*	52.68	89.68	99.26	80.46	62.72	90.58	99.05	84.11
			Focal	62.34	88.00	98.45	82.93	44.60	84.86	99.28	76.25	62.57	90.83	99.21	84.21
			Dice	60.45	87.29	97.85	81.86	61.24	88.83	98.17	82.74	60.52	87.88	97.97	82.12
			Weighted CE	60.58	84.89	97.78	81.09	53.45	90.73	99.52	81.23	60.84	86.33	98.24	81.80
			Weighted Focal	61.25	85.74	98.02	81.67	44.27	85.77	99.50	76.51	61.55	87.42	98.58	82.52
			Weighted Dice	60.21	87.00	97.74	81.65	60.72	88.17	97.98	82.29	60.27	87.46	97.83	81.86
			Fusion	61.52	88.39	98.38	82.76	58.94	92.55	99.37	83.62	61.67	90.45	98.91	83.68
4-Class (Ours)	**FCN-based**	∼295K	CE	64.55	89.21	98.39	84.05	54.60	89.68	99.23	81.17	64.87	91.81	99.06	85.25
			Focal	64.10	88.86	98.32	83.76	46.64	86.01	99.26	77.30	64.34	91.65	99.11	85.03
			Dice	64.37	88.68	98.37	83.81	65.17	90.13	98.59	84.63	64.57	89.14	98.46	84.06
			Weighted CE	63.78	87.52	98.16	83.15	54.77	90.50	99.42	81.56	64.12	89.43	98.71	84.09
			Weighted Focal	63.68	87.71	98.19	83.20	48.18	87.10	99.45	78.24	64.05	89.72	98.80	84.19
			Weighted Dice	64.21	88.57	98.30	83.69	65.08	90.10	98.53	84.57	64.44	89.06	98.39	83.96
			Fusion	64.68	88.48	98.33	83.83	59.83	91.77	99.28	83.63	65.00	90.72	98.91	84.87
	SSP - VGG16	∼24M	CE	47.36	81.02	98.23	75.54	32.20	81.80	99.52	71.18	47.44	84.20	99.06	76.90
			Focal	47.17	81.46	98.18	75.60	28.51	79.66	99.53	69.23	47.21	8.458	99.05	76.95
			Dice	52.83	80.12	97.17	76.71	54.13	84.14	97.95	78.74	52.99	81.45	97.49	77.31
			Weighted CE	52.80	83.54	97.95	78.10	37.51	85.04	99.61	74.05	52.99	81.45	97.49	77.31
			Weighted Focal	47.24	81.03	97.92	75.40	28.07	80.15	99.61	69.28	47.39	82.85	98.42	76.22
			Weighted Dice	43.54	74.56	96.45	71.52	42.80	79.25	97.48	73.17	43.63	76.54	96.93	72.37
			Fusion	49.36	80.54	97.82	75.91	38.66	84.94	99.59	74.39	49.52	83.31	98.57	77.14
	MFM (FFP + SSP) - VGG16	∼24M	CE	61.52	88.90	98.67	83.03	45.72	87.01	99.54	77.42	61.69	91.27	99.34	84.10
			Focal	60.99	88.45	98.65	82.69	37.41	82.76	99.55	73.24	61.08	90.85	99.34	83.75
			Dice	59.73	88.43	98.65	82.27	61.66	90.50	98.94	83.70	60.42	90.75	99.30	83.49
			Weighted CE	57.15	87.28	98.52	80.98	41.46	86.51	99.61	75.86	57.54	88.94	98.99	81.83
			Weighted Focal	57.90	87.35	98.49	81.24	36.60	82.71	99.60	72.97	58.35	89.05	98.97	82.12
			Weighted Dice	58.14	87.67	98.62	81.48	60.19	90.31	98.98	83.16	58.82	90.36	99.37	82.85
			Fusion	59.80	88.33	98.62	82.25	51.14	90.13	99.59	80.28	60.46	90.25	99.18	83.30
	SSP - InceptionV3	∼30M	CE	72.82	92.44	98.73	87.99	63.32	92.91	99.55	85.26	72.77	94.90	99.29	88.99
			Focal	72.20	92.14	98.69	87.68	56.95	90.34	99.54	82.28	72.18	94.86	99.32	88.79
			Dice	71.11	91.11	98.55	86.92	71.54	93.53	99.07	88.05	71.11	92.22	98.79	87.37
			Weighted CE	70.32	90.53	98.34	86.39	61.39	92.52	**99.63**	84.52	70.35	92.15	98.72	87.07
			Weighted Focal	71.64	91.06	98.39	87.03	56.10	90.48	99.60	82.06	71.62	92.68	98.79	87.69
			Weighted Dice	71.96	91.60	98.59	87.39	72.15	93.29	98.96	88.14	71.92	92.35	98.76	87.68
			Fusion	71.19	91.10	98.51	86.93	65.80	93.97	99.59	86.45	71.18	93.32	99.01	87.84
	MFM (FFP + SSP) - InceptionV3	∼30M	CE	73.10	92.66	98.77	88.18	63.48	92.89	99.55	85.31	73.05	94.89	99.36	**89.10**
			Focal	72.80	92.50	98.75	88.01	57.47	90.58	99.54	82.53	72.77	94.74	99.35	88.95
			Dice	72.56	92.20	98.70	87.82	72.38	93.60	99.00	88.33	72.52	94.73	99.37	88.87
			Weighted CE	72.66	91.90	98.54	87.70	62.65	93.04	99.62	85.10	72.63	93.31	98.94	88.29
			Weighted Focal	72.55	92.13	98.62	87.77	59.35	91.64	99.59	83.53	72.50	93.77	99.07	88.45
			Weighted Dice	72.59	92.31	98.70	87.87	72.60	94.00	99.07	88.56	72.54	94.60	99.32	88.82
			Fusion	72.55	92.25	98.71	87.83	65.57	93.49	99.53	86.19	72.49	94.62	99.35	88.82
	SSP - ResNet34	∼24M	CE	73.02	92.27	98.71	88.00	63.68	92.57	99.55	85.27	72.97	94.71	99.27	88.98
			Focal	72.74	92.26	98.71	87.90	58.54	90.95	99.55	83.01	72.71	94.88	99.32	88.97
			Dice	72.40	91.91	98.65	87.65	72.62	93.38	98.98	88.33	72.35	92.55	98.79	87.90
			Weighted CE	72.43	91.34	98.45	87.40	62.94	92.97	**99.63**	85.18	72.43	92.82	98.80	88.02
			Weighted Focal	72.39	91.38	98.43	87.40	58.85	91.38	99.61	83.28	72.35	92.94	98.81	88.03
			Weighted Dice	71.86	91.89	98.65	87.47	71.99	93.32	98.96	88.09	71.79	92.56	98.80	87.72
			Fusion	72.96	91.88	98.60	87.81	68.64	94.86	99.58	87.69	72.92	94.08	99.10	88.70
	MFM (FFP + SSP) - ResNet34	∼24M	CE	72.81	92.56	98.78	88.05	63.04	92.94	99.55	85.17	72.75	**94.93**	99.39	89.02
			Focal	73.04	92.46	98.75	88.08	53.02	89.04	99.55	80.54	73.00	94.75	99.35	89.03
			Dice	72.96	92.38	98.72	88.02	73.16	93.35	98.93	88.48	72.93	94.79	99.36	89.03
			Weighted CE	72.96	91.96	98.69	87.87	64.49	92.47	99.56	85.51	72.90	94.19	99.27	88.79
			Weighted Focal	73.18	92.10	98.63	87.97	54.96	89.71	99.60	81.42	73.16	93.72	99.06	88.65
			Weighted Dice	72.78	92.32	98.71	87.94	72.95	93.66	99.00	88.53	72.75	94.67	99.34	88.92
			Fusion	**73.26**	92.45	98.73	88.15	68.38	94.85	99.56	87.60	73.21	94.59	99.31	89.04

Table 6: IoU performance (%) on SignaTR6K dataset. Partial results from this table was presented in Table 2 and this table presents the complete results. The maximum value of a column (i.e., class) is underlined, and the overall maximum of a class with different post-processing is denoted in bold and underlined. For example, the best mean IoU for the SignaTR6K dataset is for CE loss, with CRFH, and MFM-InceptionV3 architecture at **89.10**. The best performing configuration of prior work, i.e., excluding results for Fusion loss and CRFH, marked with (*), is 83.02.

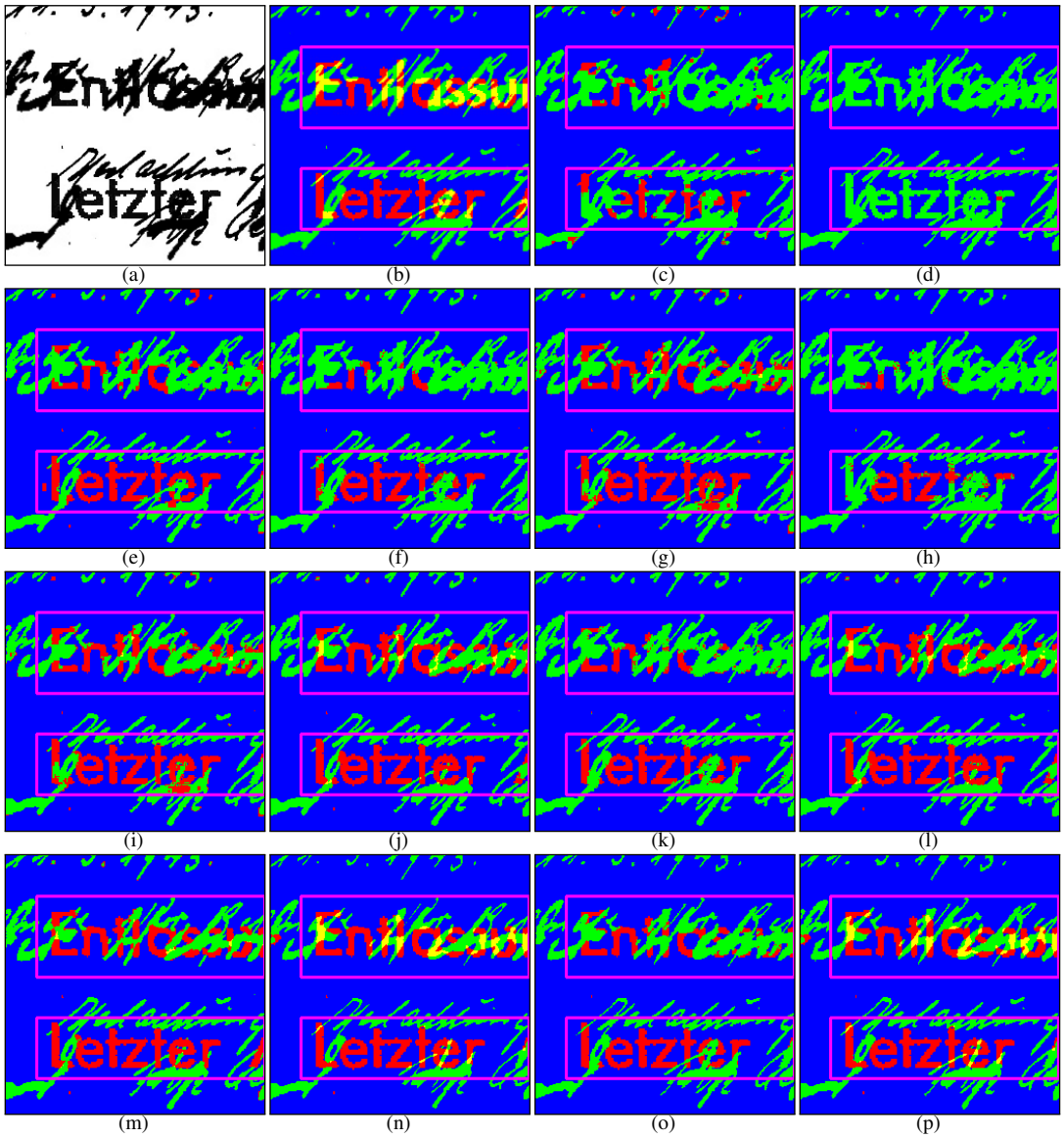

Figure 9: Example visual comparisons on the test set of the WGM-SYN dataset for our approach compared to ground through and prior works. (a) Input image; (b) Ground truth; (c) & (d) 3-class FCN-based [11] with CE loss without (c) and with (d) CRF post-processing; (e) & (f) 3-class FCN-based [35] with CE loss without (e) and with (f) CRF post-processing; (g), (h), & (i) Our FCN-based 4-class formulation with CE loss without CRF (g), with CRF (h), and with CRFH (i); (j), (k), & (l) SSP-ResNet34 with CE loss without CRF (j), with CRF (k), and with CRFH (l); (m) MFM-ResNet34 with CE loss without CRF; (n), (o), & (p) MFM-ResNet34 with Fusion loss without CRF (n), with CRF (o), and with CRFH (p);

Figure 10: Additional visual results on the test set of the SignaTR200 dataset for our approach compared to ground through and prior works. (a) Input image; (b) Ground truth; (c) & (d) 3-class FCN-based [11, 35] with CE loss without (c) and with (d) CRF post-processing; (e), (f), & (g) Our FCN-based 4-class formulation with CE loss without CRF (e), with CRF (f), and with CRFH (g); (h), (i), & (j) SSP-ResNet34 with CE loss without CRF (h), with CRF (i), and with CRFH (j); (k), (l), & (m) MFM-ResNet34 with CE loss without CRF (k), with CRF (l), and with CRFH (m); (n), (o), & (p) MFM-ResNet34 with Fusion loss without CRF (n), with CRF (o), and with CRFH (p);